11th ANKARA INTERNATIONAL AEROSPACE CONFERENCE **AIAC-2021-110**
8-10 September 2021 - METU, Ankara TURKEY

MODELING THE FLAPPING MOTION VIA QUASI-STEADY APPROACH AND CONTROLLING THE LONGITUDINAL DYNAMICS OF A FLAPPING WING MAV

Ozgun Calis[1] and Dilek Funda Kurtulus[3]
Middle East Technical University
Ankara, Turkey

Kutluk Bilge Arikan[2]
TED University
Ankara, Turkey

ABSTRACT

An aerodynamic model in order to simulate and control the flapping-wing micro air vehicle based on the quasi-steady approach and blade element theory is developed to calculate the instantaneous aerodynamic forces and moments. The system dynamics of a 2-D flapping-wing MAV in hover mode are modeled. Control simulations are done for hover, take-off, forward flight and landing conditions. Linear Quadratic Regulator (LQR) and Coefficient Diagram Method (CDM) are used to stabilize the flapping-wing system. The effectiveness of the controllers are compared in the means of disturbance rejection, response speed, and controller response. By using the stroke plane angle and the flapping frequency as the control inputs, six state variables of the system are stabilized. Position commands are tracked with an integral tracker at low-speed flights.

INTRODUCTION

Since flying insects can hover and realize rapid maneuvers when necessary, imitating insect behaviors has become an exciting subject for engineers [Kurtulus, 2019]. Consequently, the number of studies on flapping wing Micro Air Vehicles (MAVs) has grown significantly in recent years [Ward et al., 2017].

The aerodynamic characteristics of flying insects are different from the aircraft and helicopters flying at high Reynolds numbers [Kurtulus 2011a; Kurtulus 2011b; Kurtulus 2015]. Therefore, the wing morphology, wing kinematics, and unsteady aerodynamics of the flapping motion must be investigated to perform an insect-like flight [Akay et al., 2007; Kurtulus et al., 2004; Kurtulus et al., 2005; Kurtulus et al., 2006a; Kurtulus et al., 2006b; Kurtulus et al., 2006c; Kurtulus et al., 2008; Kurtulus, 2009; 2018; Bektas, 2020; Bektas et al., 2020]. A frequently preferred and straightforward method to calculate unsteady forces is the quasi-steady approach [Madangopal et al., 2006; Wissa et al., 2020]. Quasi-steady estimations include the instantaneous position and velocity of the wing while other time-dependent effects such as

[1] M.Sc. Student in Aerospace Engineering Department, METU, Email: calis.ozgun@metu.edu.tr
[2] Asst. Prof. in Mechanical Engineering Department, TEDU, Email: kutluk.arikan@tedu.edu.tr
[3] Prof. in a Aerospace Engineering Department, Email: kurtulus@metu.edu.tr

wake-capture, wing-wing interactions, wing-body interactions are neglected [Wright and Cooper, 2015; Bhatia et al., 2012]. However, it is commonly used in flapping wing control applications due to its simplicity and low computational costs [Lee et al., 2015; Banazadeh and Taymourtash, 2016; Al-Mahasneh et al., 2017].

The delayed stall and the Wagner effect are the two effects that suppress each other's influence on lift production [Weis-Fogh, 1972]. [Han and Han, 2019] stated that the downwash created by a wing has an attenuating effect on the vortex created by the side wing, and this is a stabilizing effect when there is a lateral disturbance. Quasi-steady approximations cannot model these effects mentioned above. On the other hand, since they have opposite effects, even they are not included in the calculations, it is still convenient to use a quasi-steady aerodynamic model during dynamical stability and control analyses [Taha et al., 2012]. [Sane and Dickinson, 2002] revealed that despite the unsteady forces are ignored during quasi-steady calculations, one can obtain close results to the experimental results via quasi-steady estimations.

In the current study, an aerodynamic model based on quasi-steady estimations and blade element theory is developed to calculate the aerodynamic forces created during the flapping motion. The model is based on the studies of [Kim et al., 2015]. The model uses the translational forces, the rotational forces, and the added-mass effect to calculate the total forces. The effects of the wake-capture, wing-wing interactions, wing-body interactions, and the spanwise components of the flow are ignored. Wing's thickness is assumed to be infinitesimally small during calculations since the thickness of the insects' wings that are flying at low Reynolds numbers is very small [Kurtulus, 2016].

The open-loop dynamics of a flapping wing MAV are reported to be unstable [Taylor and Thomas, 2003; Sun and Xiong, 2005; Çalış et al., 2019]. There are various studies on stabilizing flapping-wing MAVs using different linear control methods. PID is a successful method in flapping-wing MAV control applications [Zhang et al., 2016]. [Nakatani et al., 2016] tested the PID and the PI controllers and proved the usability of these types of controllers in the existence of disturbance. [Hines et al., 2011] used PID controllers for attitude and altitude control. [Fei et al., 2019] used cascaded PD and PID controllers successfully in simulations and flight tests. Nonlinear control methods are also employed for controlling flapping-wing MAVs in various studies [Banazadeh and Taymourtash, 2016; Wissa et al., 2020; Hashemi et al., 2020].

[Deng et al. 2006, Bhatia et al. 2012, Biswal 2015, P.Hyun et al., 2021] used LQR to stabilize the dynamics of flapping wing MAVs. [Abbasi and Mahmood., 2019] successfully used LQR to stabilize the unstable dynamics of a nature-inspired flapping wing UAV. [Biswal et al., 2019] designed an LQR controller for stabilizing the rigid body dynamics of a flapping wing MAV. Then they proved the convenience of the controller by testing it with the model that includes all the rigid body dynamics, rigid wing dynamics, and wing kinematics. [Zhang et al. 2016] used an LQR controller, a PID controller, and a nonlinear controller for wing trajectory tracking. Compared to the other control approaches, the LQR controller tracked the command with less input effort with less precision.

The Coefficient Diagram Method (CDM) is an algebraic approach to the control theory in the middle of classical control and modern control [Manabe, 1998]. It is a linear control method in which the desired characteristic equation is obtained by solving simple algebraic equations [Kara, 2014]. It is used in various UAV applications [Hirokawa, 2004; Giernacki, 2017]. However, no flapping-wing study has been encountered with this method in the literature yet.

In the current study, an LQR controller and a CDM-based controller are employed for stabilization, and integral trackers are utilized for position command tracking. The longitudinal dynamics of the flapping-wing MAV are trimmed at hovering flight. The wing kinematics are considered in the dynamic stability analysis by including the aerodynamic model in the linear time-invariant system by getting linearized around the trim condition. However, the rigid wing dynamics are not modeled separately and are assumed to be involved in the rigid body dynamics. [Lee et al., 2015] used the stroke plane angle and the flapping frequency to stabilize a flapping-wing MAV in hover. In the current study, the forward-backward motion of the

flapping-wing MAV is controlled by changing the stroke plane angle whereas, the upward-downward movement is controlled by altering the flapping frequency.

The hawkmoth Manduca sexta (MS) is being inspired for modeling the body dynamics and the flapping motion. A simplified hawkmoth wing model with a span of 52.25 mm from the literature is used [Usherwood and Ellington, 2002]. The morphological parameters of the body are obtained from [Kim et al., 2015].

MODELING OF A FLAPPING-WING MAV

Coordinate Definitions

Four orthonormal and right-handed coordinate frames are defined to clarify the body dynamics and wing kinematics, as illustrated in Figure 1. The Global Frame (X_G, Y_G, Z_G), is fixed to any point on Earth, the X_G-axis is pointing north, the Z_G-axis is pointing to the center of the Earth, and the Y_G-axis is perpendicular to the $X_G - Z_G$ frame satisfying the right-hand rule. The Body Fixed Coordinate Frame (X_B, Y_B, Z_B), is fixed to the insect's center of gravity. The X_B-axis is along the insect's body and makes an angle of Θ with the horizontal plane which is the body pitch angle. The Z_B-axis is perpendicular to the X_B-axis, as shown in Figure 1a, and the Y_B-axis is perpendicular to the $X_B - Z_B$ plane, satisfying the right-hand rule. The Stroke Plane Frame (X_{sp}, Y_{sp}, Z_{sp}) is used for analyzing the flapping motion. The Wing Fixed Frame (X_W, Y_W, Z_W) is fixed to the wing root, as shown in Figure 1c. The X_W-axis is throughout the chord, the Z_W-axis is along the span and pointing the wingtip. The Y_W-axis is perpendicular to the X_W-Z_W plane. The stroke plane angle (β) is the angle between the X_{sp}-axis and the X_G-axis initially when the insect's body is aligned with the X_G-axis, as shown in Figure 1b.

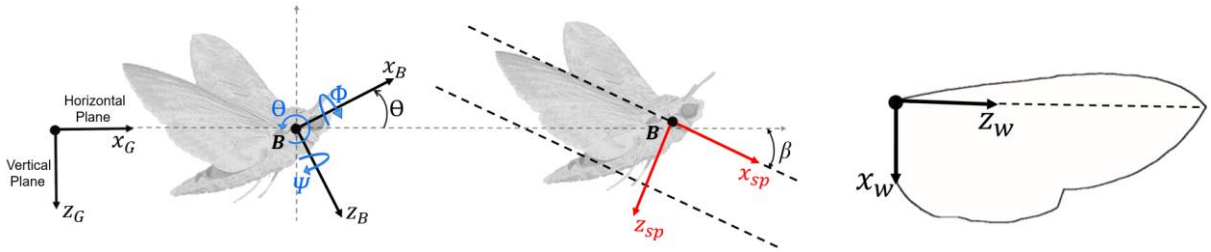

(a) (b) (c)

Figure 1: Wing and body kinematic definitions and coordinate systems

Aerodynamic Model

To manipulate and control their body, insects change the aerodynamic forces by altering their wing kinematics. Therefore, there is a need to investigate the aerodynamic forces created during the flapping motion to control a flapping wing MAV. In this study, a quasi-steady model with the blade element method is used to calculate the aerodynamic forces and moment created during the flight. The model is developed based on the model proposed by [Kim et al., 2015]. The wing is separated into equal strips along the span, and instantaneous aerodynamic forces and moment are computed on each strip independently. Finally, the effects of the aerodynamic forces and moment acting on each strip to the wing root are calculated. During the flapping motion, the instantaneous aerodynamic forces acting on a single strip when there is no skin friction are the sum of four forces: translational, rotational, forces due to the inertia of the added mass of the air and the wake-capture effect [Sane and Dickinson, 2002]. Since the wake-capture effect is highly unsteady, it is not possible to model it with a quasi-steady approach. Therefore, it is neglected, and the instantaneous forces and moment on a strip are calculated as in Equation 1.

$$F_{instantaneous} = F_{translation} + F_{rotation} + F_{added-mass} \quad (1)$$

The components of Equation 1 are calculated as the way proposed by [Kim et al., 2015]. The wing shape is introduced to the code simply by two functions shown in Equations 2-3, one representing the leading edge and the other representing the trailing edge, as shown in Figure 2.

$$X_{leading} = -1.246 \cdot 10^{9} \cdot z^{8} - 7.249 \cdot 10^{7} \cdot z^{7} + 3.105 \cdot 10^{7} \cdot z^{6} - 2.271 \cdot 10^{6} \cdot z^{5} + 6.48 \cdot 10^{4} \cdot z^{4} - 553.4 \cdot z^{3} - 7.91 \cdot z^{2} + 0.295 \cdot z + 2.033 \cdot 10^{-5} \quad (2)$$

$$X_{trailing} = 5.783 \cdot 10^{10} \cdot z^{8} - 1.567 \cdot 10^{10} \cdot z^{7} + 1.698 \cdot 10^{9} \cdot z^{6} - 9.458 \cdot 10^{7} \cdot z^{5} + 2.895 \cdot 10^{6} \cdot z^{4} - 4.857 \cdot 10^{4} \cdot z^{3} + 440.7 \cdot z^{2} - 2.238 \cdot z - 0.01382 \quad (3)$$

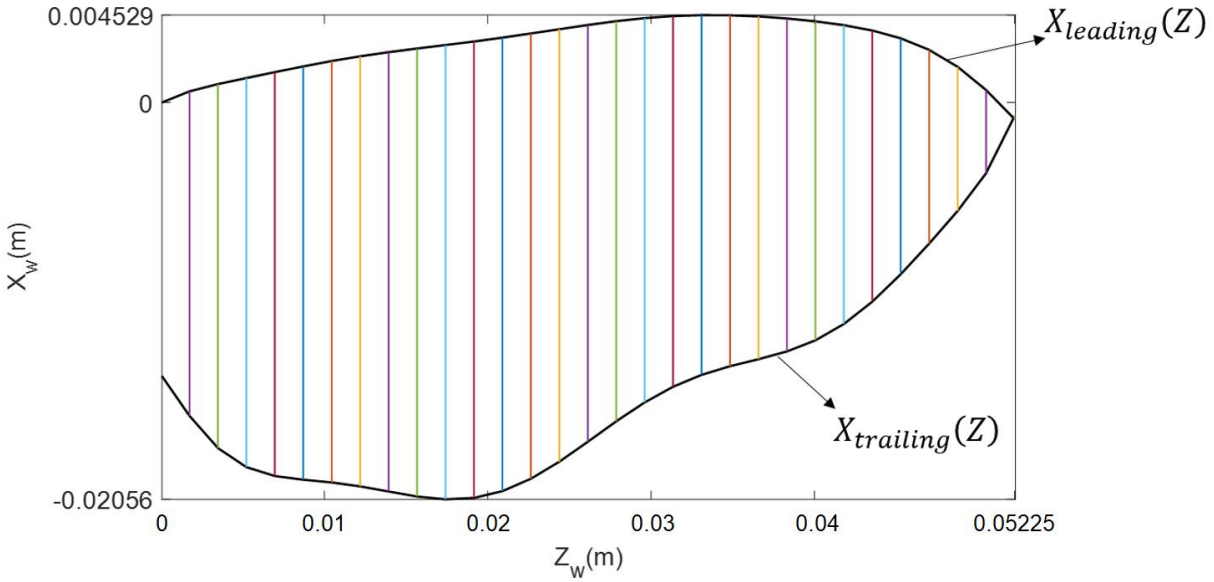

Figure 2: Wing model with 30 equal strips

As the number of strips increased, the mean value of aerodynamic forces during one wing-beat converged to a final value. Consequently, dividing the wing into 700 pieces is found to be satisfactory. The wing used by [Kim et al., 2015] and the wing used in the current study, which is divided into 700 equal strips, are presented in Figure 3.

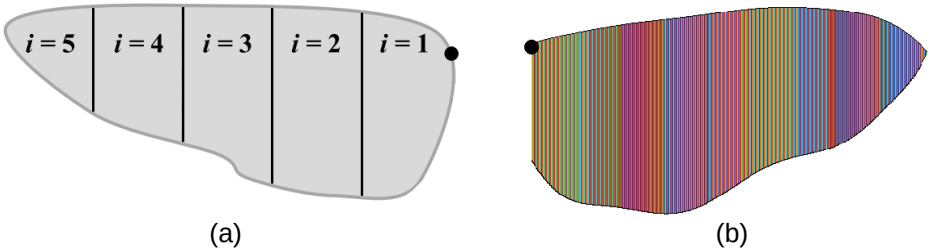

(a) (b)

Figure 3: (a) Hawkmoth Manduca Sexta wing model with 5 strips [Kim et al., 2015] (b) Wing model used in the current study with 700 strips

Calculations are done for each strip of the wing. Components of Equation 1 are obtained from [Kim et al., 2015] and shown in Equation 4.

$$F_{instantaneous,i} = \begin{bmatrix} L_i \\ D_i \\ M_i \end{bmatrix} = \begin{bmatrix} L_{T,i} \\ D_{T,i} \\ M_{T,i} \end{bmatrix} + \begin{bmatrix} L_{R,i} \\ D_{R,i} \\ M_{R,i} \end{bmatrix} + \begin{bmatrix} L_{a,i} \\ D_{a,i} \\ M_{a,i} \end{bmatrix} = \begin{bmatrix} C_{L,i}\frac{\rho}{2}V_i^2 c_i dr \\ C_{D,i}\frac{\rho}{2}V_i^2 c_i dr \\ C_{M,i}\frac{\rho}{2}V_i^2 c_i^2 dr \end{bmatrix} + \begin{bmatrix} C_{R,i}\rho\dot{\alpha}_i V_i c_i^2 dr \cdot cos\alpha \\ C_{R,i}\rho\dot{\alpha}_i V_i c_i^2 dr \cdot sin\alpha \\ C_{R,i}\rho\dot{\alpha}_i V_i c_i^2 dr \cdot \varepsilon_i \end{bmatrix} + \begin{bmatrix} \frac{\pi}{4}\rho c_i^2(\ddot{\Phi}R) sin\alpha dr \cdot cos\alpha \\ \frac{\pi}{4}\rho c_i^2(\ddot{\Phi}R) sin\alpha dr \cdot sin\alpha \\ \frac{\pi}{4}\rho c_i^2(\ddot{\Phi}R) sin\alpha dr \cdot \varepsilon_i \end{bmatrix} \quad (4)$$

where, ρ is the air density and taken as $1.225\ kg/m^3$, V_i is the inflow velocity, c_i is the strip's chord length, dr is the width of the strip, ε_i, is the distance between the half chord line and the wing pitching axis Z_w, and acts as a moment arm. R is the distance of the strip from the wing root. The aerodynamic coefficients ($C_{L,i}$, $C_{D,i}$, $C_{M,i}$), are curve fitted from experimental results given by [Han et al., 2015] as functions of the effective angle of attack. The curve fitted equations are given in Equations 5-7. $C_{R,i}$ is taken from [Kim et al., 2015] and shown in Equation 8.

$$C_L(\alpha_i) = 0.8456sin(0.02086\alpha_i + 1.265) + 0.8452sin(0.04803\alpha_i - 1.181) + 0.04764sin(0.1169\alpha_i - 1.101) \quad (5)$$

$$C_D(\alpha_i) = 2.941sin(0.01935\alpha_i - 0.171) + 0.7002sin(0.06062\alpha_i - 3.867) + 0.1118sin(0.1246\alpha_i - 3.36) \quad (6)$$

$$C_M(\alpha_i) = 0.7671sin(0.02421\alpha_i + 2.534) + 0.3185sin(0.0747\alpha_i - 2.009) + 0.1051sin(0.1418\alpha_i - 8.034) + 0.04902sin(0.2054\alpha_i - 7.459) \quad (7)$$

$$C_{R,i} = \pi\left(0.75 - \frac{x_i}{c_i}\right) \quad (8)$$

where, x_i is the distance between the leading edge of the strip and the wing pitching axis (Z_w). V_i and α_i calculations are shown by [Kim and Han, 2014].

The wing kinematics used for the dynamic stability analysis are similar to a real hawkmoth Manduca Sexta, taken from [Kim and Han, 2014], and represented in Figure 4.

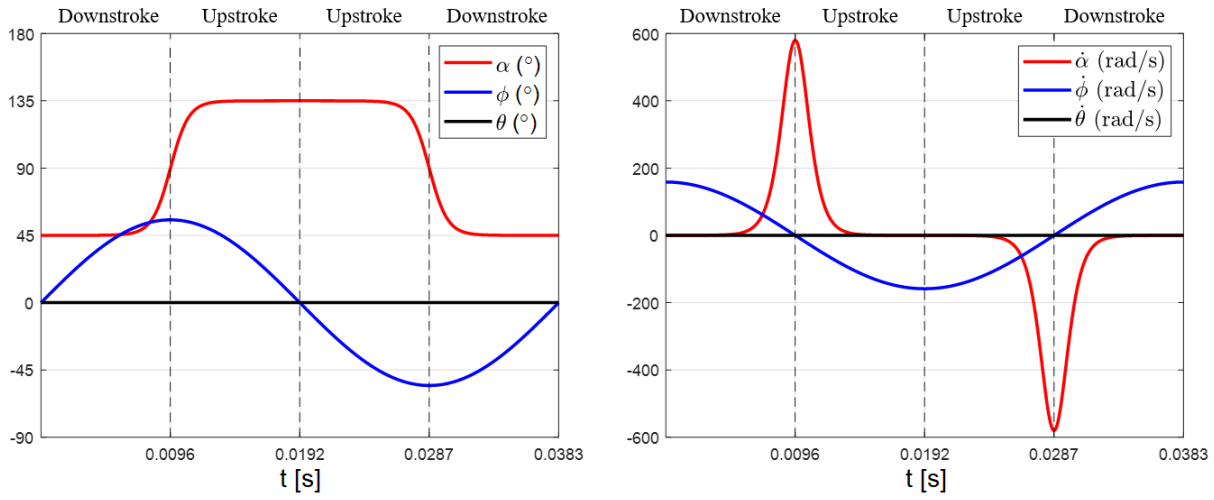

(a) (b)

Figure 4: (a) Angular positions of the wing for one flapping period (b) Angular velocities of the wing for one flapping period

In Figure 4, α is the feathering angle and is equal to the angle of attack when there is no external incoming flow and the insect is hovering. ϕ is the stroke positional angle, and θ is the elevation angle. Note that the elevation angle (θ) is different from the body pitch angle (Θ). Manduca sextas generally do not flap their wings with notable amplitudes around the elevation angle (θ) [Willmott and Ellington, 1997]. Therefore, in the current study, the elevation angle (θ) is set to zero as shown in Figure 4.

Aerodynamic Model Validation:

The results obtained from the aerodynamic model are compared with the CFD results for a pure-plunge motion which has the kinematics represented in Figure 5. The validation case is obtained from [Bektas et al., 2019].

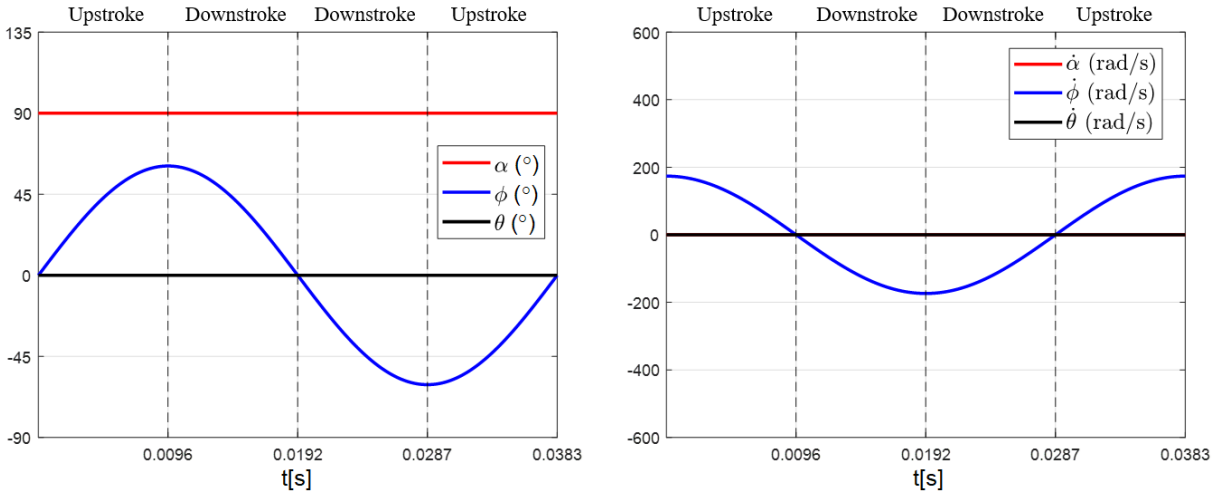

(a) (b)

Figure 5: Validation Case (a) Angular positions of the wing for one period (b) Angular velocities of the wing for one flapping period

Keep in mind that since the validation case is a pure-plunge motion, the angle of attack is constant throughout the flapping motion and kept at 90° as shown in Figure 5. The elevation angle (θ) is 0°, and the stroke plane angle is 15°.

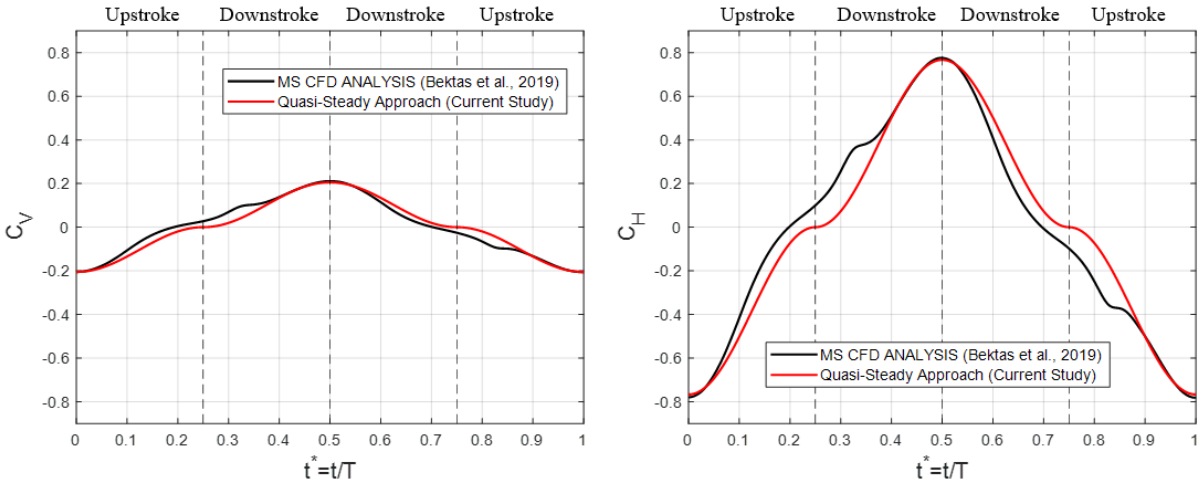

(a) (b)

Figure 6: Comparison of the Aerodynamic model results and the CFD results (a) vertical force coefficient (b) horizontal force coefficient

The results obtained with the aerodynamic model have shown a good agreement with the CFD results during a flapping cycle. The most considerable disagreement between the results are received after the stroke reversals, at near 0.3T and 0.8T for both vertical and horizontal forces. The difference disappears as the wing's motion continues and arises back as the next stroke reversal approaches. This difference might be caused because the aerodynamic model based on the quasi-steady approach cannot consider the downwash, whereas the CFD method can. Downwash created due to the trace of vortices from the previous flapping cycle acts on the wing during the reverse stroke. Note that the model underestimates the forces at 0.3T while overestimating the forces at 0.8T, which yields the total error to vanish at the cycle-averaged evaluations.

System Modeling

The system is trimmed in hover using the Flat Earth, Body-Axes 6 degree of freedom equations taken from [Stevens et al., 2015] and 6 state equations are obtained as shown in Equation 9-14.

$$\dot{x_1} = \dot{x_B} = u\cos\theta + w\sin\theta \tag{9}$$

$$\dot{x_2} = \dot{u} = -g\sin\theta - qw + \frac{F_{ae_x}}{m} \tag{10}$$

$$\dot{x_3} = \dot{x_B} = -u\sin\theta + w\cos\theta \tag{11}$$

$$\dot{x_4} = \dot{w} = -g\cos\theta - qu + \frac{F_{ae_z}}{m} \tag{12}$$

$$\dot{x_5} = \dot{\theta} = q \tag{13}$$

$$\dot{x_6} = \dot{q} = \frac{M_{Y_B}}{J_Y} \tag{14}$$

where, the state variables are $x = [x_B \ u \ z_B \ w \ \theta \ q]^T$, and $\frac{F_{ae_x}}{m} = \hat{F}_{XB}, \frac{F_{ae_z}}{m} = \hat{F}_{ZB}, \frac{M_{Y_B}}{J_Y} = \hat{M}_{YB}$. After the 6 state equations are obtained, the Jacobian Matrix method is used to get the system matrix A. The system matrix A with the stability derivative terms are presented in Equation 15.

$$A = \begin{bmatrix} 0 & \cos(\theta) & 0 & \sin(\theta) & 0 & 0 \\ 0 & \partial\hat{F}_{XB}/_{\partial \mathrm{u}} & 0 & \partial\hat{F}_{XB}/_{\partial \mathrm{w}} & \partial\hat{F}_{XB}/_{\partial\theta} - g & \partial\hat{F}_{XB}/_{\partial \mathrm{q}} \\ 0 & -\sin(\theta) & 0 & \cos(\theta) & 0 & 0 \\ 0 & -\partial\hat{F}_{ZB}/_{\partial \mathrm{u}} & 0 & -\partial\hat{F}_{ZB}/_{\partial \mathrm{w}} & -\partial\hat{F}_{ZB}/_{\partial\theta} - g & -\partial\hat{F}_{ZB}/_{\partial \mathrm{q}} \\ 0 & 0 & 0 & 0 & 0 & 1 \\ 0 & \partial\hat{M}_{YB}/_{\partial \mathrm{u}} & 0 & \partial\hat{M}_{YB}/_{\partial \mathrm{w}} & \partial\hat{M}_{YB}/_{\partial\theta} & \partial\hat{M}_{YB}/_{\partial \mathrm{q}} \end{bmatrix} \quad (15)$$

Small perturbations are applied to the state variables, and the slopes of the changes of the cycle-averaged force and moment terms are regarded as the stability derivatives as proposed by [Lee et al., 2015]. The aerodynamic forces are calculated with the aerodynamic model based on the quasi-steady estimations as presented earlier, and the system matrix A is obtained as shown in Equation 16.

$$\mathrm{A} = \begin{bmatrix} 0 & 0.7683 & 0 & 0.6401 & 0 & 0 \\ 0 & -1.953 & 0 & 0.7775 & -5.9245 & -0.0533 \\ 0 & -0.6401 & 0 & 0.7683 & 0 & 0 \\ 0 & -2.3930 & 0 & 0.9613 & -6.5739 & -0.0621 \\ 0 & 0 & 0 & 0 & 0 & 1 \\ 0 & 65.6034 & 0 & -29.0895 & 0 & 1.4521 \end{bmatrix} \quad (16)$$

The eigenvalues of the system are given in Equation 17. It is clear that the system is unstable because of the complex conjugate eigenvalue pair that has positive real parts.

$$\lambda = [0 \quad 0 \quad -5.6594 \quad \mathbf{3.0615 \pm 5.0513} \quad -0.0032] \quad (17)$$

CONTROLLER DESIGN

To obtain the control matrix B, derivatives of the six state equations are obtained with respect to two control inputs which are the stroke plane angle (*β*) and the flapping frequency (*f*). The control matrix B and the control derivatives are presented in Equation 18.

$$B = \begin{bmatrix} 0 & 0 \\ \partial\delta\hat{F}_{XB}/_{\partial\delta\beta} & \partial\delta\hat{F}_{XB}/_{\partial\delta f} \\ 0 & 0 \\ \partial\delta\hat{F}_{ZB}/_{\partial\delta\beta} & \partial\delta\hat{F}_{ZB}/_{\partial\delta f} \\ 0 & 0 \\ \partial\delta\hat{M}_{YB}/_{\partial\delta\beta} & \partial\delta\hat{M}_{YB}/_{\partial\delta f} \end{bmatrix} \quad (18)$$

To calculate the control derivatives, the slopes of the changes in cycle-averaged forces and moments are obtained by giving small perturbations to the control inputs. After the control derivatives are substituted, the control matrix B is obtained as shown in Equation 19.

$$B = \begin{bmatrix} 0 & 0 \\ -8.5368 & 0.2858 \\ 0 & 0 \\ -4.9804 & -0.7915 \\ 0 & 0 \\ 0 & 1.7947 \end{bmatrix} \quad (19)$$

All the system states are assumed to be measured, and the output matrix C is accepted as an identity matrix. The feedforward matrix D is taken as 0. An inner loop controller gain and an

outer loop controller gain are calculated to stabilize the system and track the position commands at low speeds. The control architecture is shown in Figure 7.

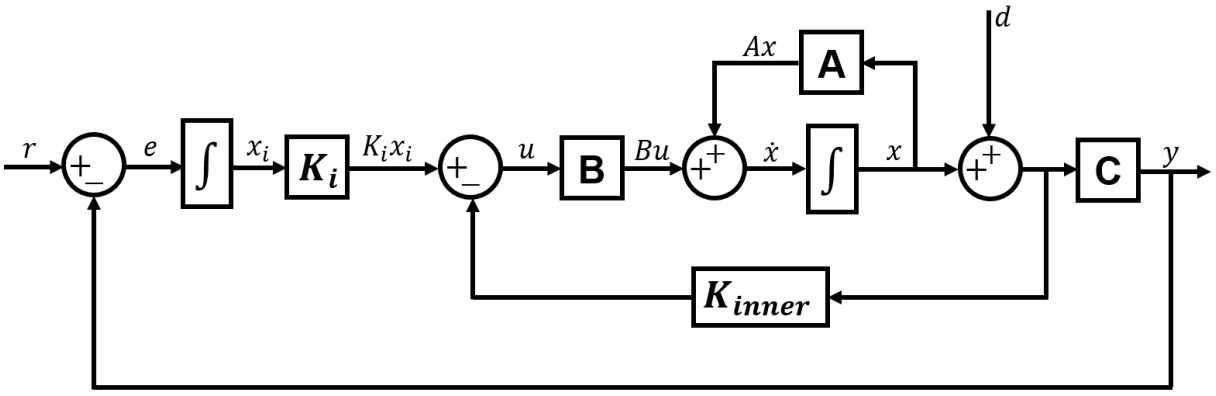

r : Reference Input
e : Error Signal
u : Controller Input
x : System States
d : Disturbance Signal
y : System Output

A: System Matrix
B: Control Matrix
C: Output Matrix
K_{inner}: Inner Controller Gain Matrix
K_i: Integral Tracker Gain Matrix

Figure 7: Block diagram representation of the LTI System with inner loop and outer loop controllers

The augmented matrices $A_{Augmented}$ and $B_{Augmented}$ are shown in Equations 20-21 respectively and used during the gain calculation phases.

$$A_{Augmented} = \begin{bmatrix} A & [0] \\ -C & [0] \end{bmatrix} \tag{20}$$

$$B_{Augmented} = \begin{bmatrix} B \\ [0] \end{bmatrix} \tag{21}$$

Controller Design with Linear Quadratic Regulator

An LQR controller is used to stabilize the system and the optimal controller gain is obtained by minimizing the cost function given in Equation 22.

$$J = \frac{1}{2}\int_0^\infty \left(x_B^T Q x_B + u_b^T R u_b\right) dt \tag{22}$$

The weight matrices Q and R are chosen as shown in Equations 23–24, respectively.

$$Q = \begin{bmatrix} 10 & 0 & 0 & 0 & 0 & 0 \\ 0 & 1 & 0 & 0 & 0 & 0 \\ 0 & 0 & 100 & 0 & 0 & 0 \\ 0 & 0 & 0 & 1 & 0 & 0 \\ 0 & 0 & 0 & 0 & 10 & 0 \\ 0 & 0 & 0 & 0 & 0 & 1 \end{bmatrix} \tag{23}$$

$$R = \begin{bmatrix} 0.001 & 0 \\ 0 & 0.001 \end{bmatrix} \tag{24}$$

The gain matrix is obtained as shown in Equation 25.

$$K = \begin{bmatrix} -19569.2 & -611.3 & 29060.8 & 740.3 & 2733.7 & 437.3 & -20936.05 & 5671.26 \\ 239555.4 & -8061.8 & 441170.4 & 13797.9 & 33081.1 & 7992.4 & -159794.74 & 167381.75 \end{bmatrix} \quad (25)$$

The values of the first six columns are used as the gain for the inner feedback loop controller, which is employed to stabilize the system. Meanwhile, the 7th and 8th column values are used as the tracker gain, which is used to track the command inputs.

The Feedback Gain (K_{inner}) and the Integral Tracker Gain (K_i) are calculated as presented in Equations 26-27.

$$K_{inner} = \begin{bmatrix} -19569.2 & -611.3 & 29060.8 & 740.3 & 2733.7 & 437.3 \\ 239555.4 & -8061.8 & 441170.4 & 13797.9 & 33081.1 & 7992.4 \end{bmatrix} \quad (26)$$

$$K_i = \begin{bmatrix} -20936.05 & 5671.26 \\ -159794.74 & 167381.75 \end{bmatrix} \quad (27)$$

Vertical take-off, hover and forward flight reference inputs are given to the system model that is linearized around the hovering condition.

The behavior of the designed system is tested against the disturbances. The disturbances that are assumed to act to flapping-wing MAV are applied to the system response, as shown in Figure 7. These signals are considered as the influence of the perturbative forces and moments acting on the system instead of the sensory noise. The frequencies of the disturbance signals are within the bandwidth of the system. The disturbance signals applied to the system are shown in Figure 8, and the response of the system to the reference inputs in the existence of disturbances is shown in Figure 9.

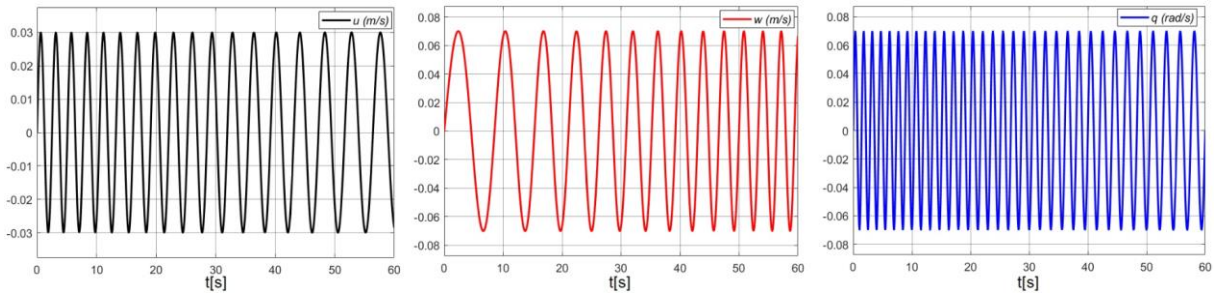

(a) (b) (c)

Figure 8: Disturbance Signals (a) applied to the linear velocity state x_b (b) applied to the linear velocity state z_b (c) applied to the pitching rate state q

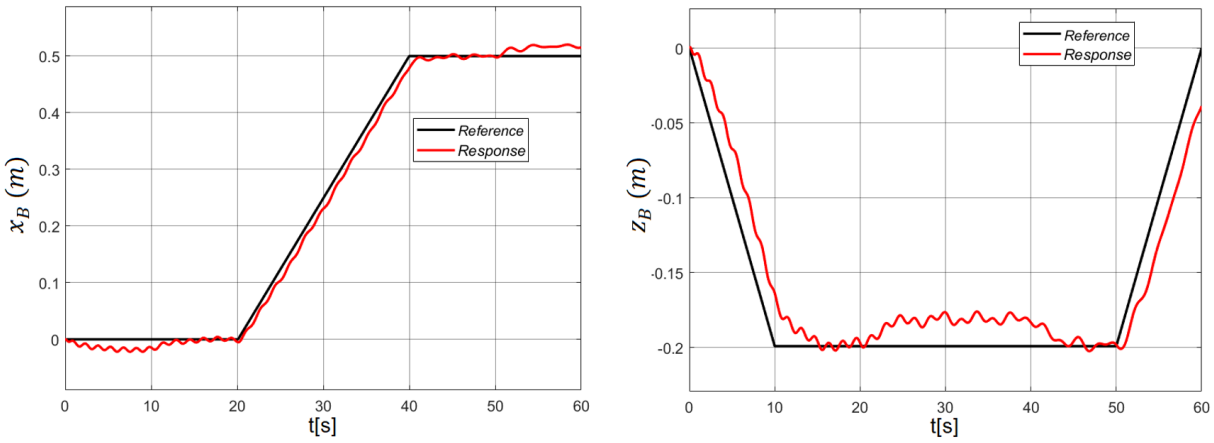

(a) (b)

Figure 9: The behavior of the system when the gain is calculated with the LQR technique (a) behavior on the horizontal plane (b) behavior on the vertical plane

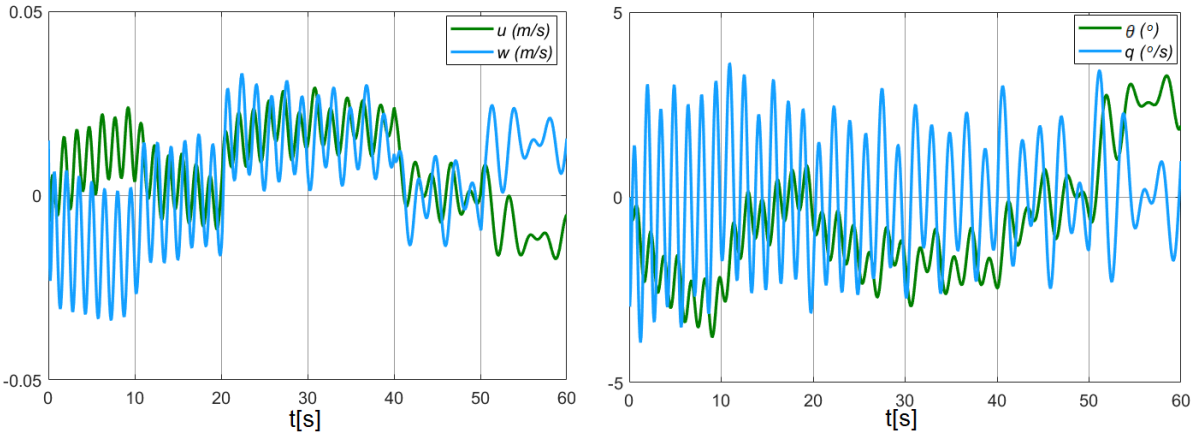

(a) (b)

Figure 10: System's other states' responses when the gain is calculated with the LQR technique (a) linear velocity (u) on the X_G-axis, and linear velocity (w) on the Z_G-axis (b) body pitch angle (θ), and body pitch rate (q)

The LQR controller maintained the stability of the flapping-wing MAV model. The system could still track the reference inputs when the disturbances are added to the linear and angular velocity responses.

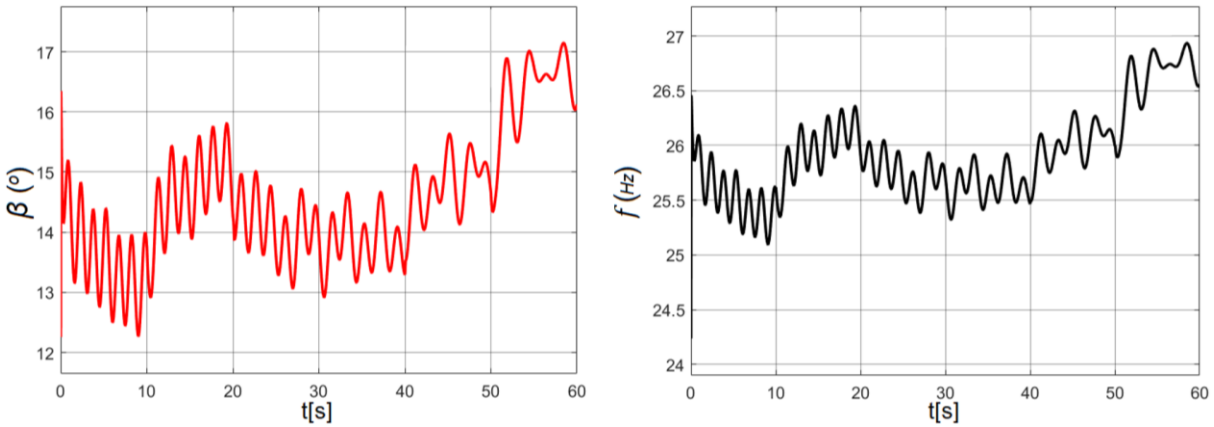

(a) (b)

Figure 11: Response of the LQR Controller (a) Changes in the stroke plane angle (*β*) (b) Changes in the flapping frequency (*f*)

Controller Design with the Coefficient Diagram Method

The same control configuration presented in Figure 7 is used but with a different tuning method called the Coefficient Diagram Method (CMD). The target characteristic equation is obtained by solving Equation 28.

$$P_m(s) = \prod_{j=1}^{n-1} \gamma_{n-j}^{j} / \tau^n \left[\left\{ \sum_{i=2}^{n} \left(\prod_{j=1}^{i-1} \frac{1}{\gamma_{i-j}^{j}} \right) (\tau s)^i \right\} + \tau s + 1 \right] \tag{28}$$

The stability index is chosen as proposed by [Kara, 2004], as shown in Equation 29. Calculations are done for the time constant $\tau = 1.6$.

$$\gamma_2 = \gamma_3 = \gamma_4 = \gamma_5 = \gamma_7 = \gamma_7 = 2$$
$$\gamma_1 = 2.5 \tag{29}$$

When the stability index given in Equation 29 are used to solve Equation 28, the desired characteristic equation is obtained as shown in Equation 30.

$$P_m(s) = 0.0000001s^8 + 0.00001s^7 + 0.0005s^6 + 0.0125s^5 + 0.15625s^4 + 0.97654s^3 + 3.05168s^2 + 4.76826s + 2.98016 \tag{30}$$

Gain calculations are done by placing the eigenvalues of the augmented A and B matrices to the roots of the characteristic equation given in Equation 30.

$$K = \begin{bmatrix} 233.70 & 5.5 & -536 & -17.4 & -63 & -12 & 312.5 & -655.6 \\ -1275.8 & -22.5 & 2545.8 & 56.8 & 314.3 & 62.7 & -1667 & 3027 \end{bmatrix} \tag{31}$$

The values of the first six columns are used as the gain for the inner feedback loop controller, and the 7th and the 8th column values are used as the tracker gain. The Feedback Gain (K_{inner}) and the Integral Tracker Gain (K_i) are presented in Equations 32-33 respectively.

$$K_{inner} = \begin{bmatrix} 233.70 & 5.5 & -536 & -17.4 & -63 & -12 \\ -1275.8 & -22.5 & 2545.8 & 56.8 & 314.3 & 62.7 \end{bmatrix} \quad (32)$$

$$K_i = \begin{bmatrix} 312.5 & -655.6 \\ -1667 & 3027 \end{bmatrix} \quad (33)$$

Figure 12 shows the response of the system to the reference inputs in the existence of disturbances. The disturbance signals that are presented in Figure 8 are applied to the system. The controller system was able to track the position commands.

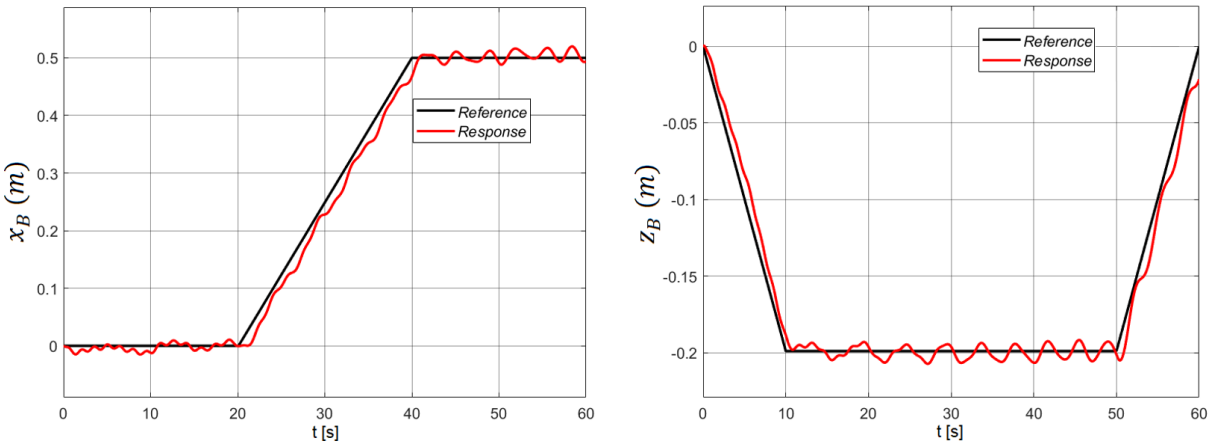

(a) (a)

Figure 12: The behavior of the system when the gain is calculated with the CDM (a) behavior on the horizontal plane (b) behavior on the vertical plane

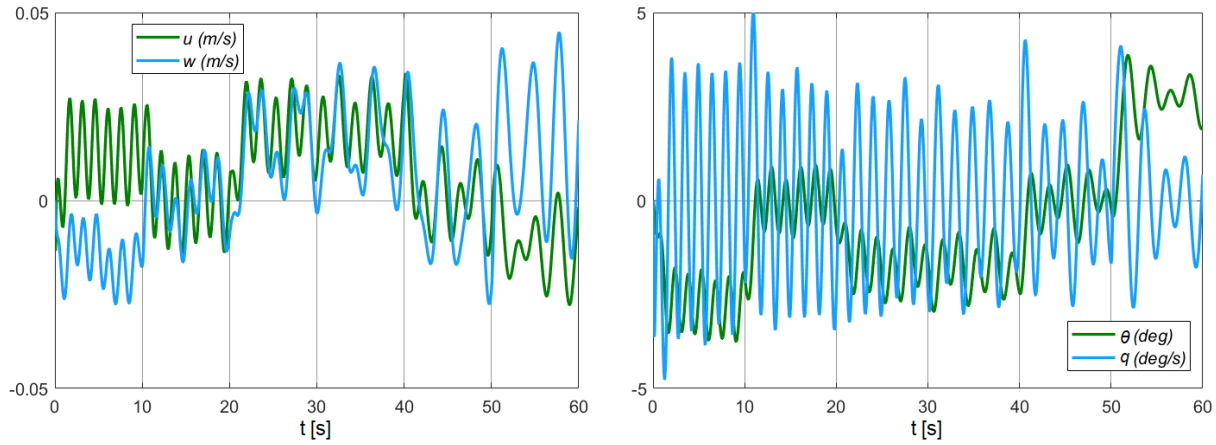

(a) (a)

Figure 13: System's other states' responses when the gain is calculated with the CDM (a) linear velocity (u) on the X_G-axis, and linear velocity (w) on the Z_G-axis (b) body pitch angle (θ), and body pitch rate (q)

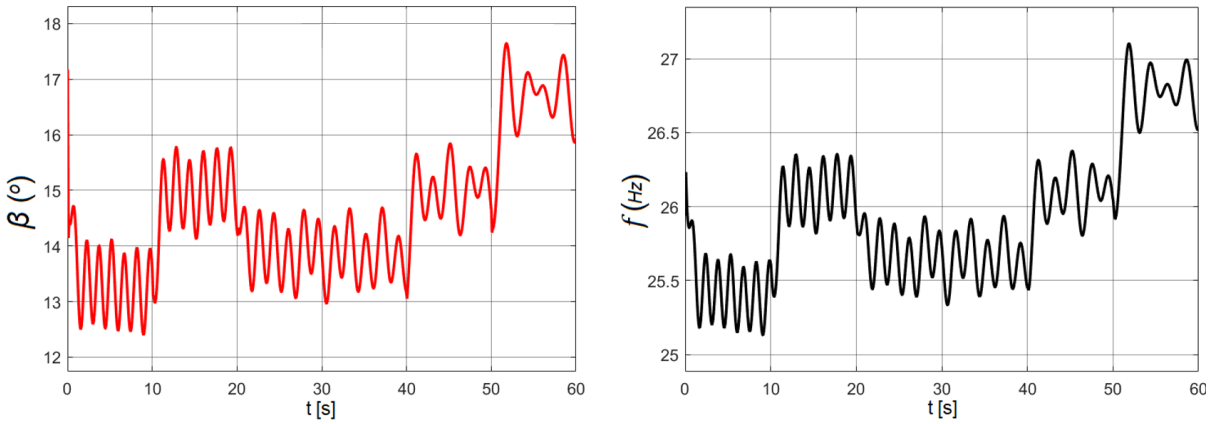

Figure 14: Response of the controller when the gains are calculated with the CDM (a) changes in the stroke plane angle (β) (b) changes in the flapping frequency (f)

DISCUSSIONS

In this section, performances of the two control methods are compared in the means of system responses and controller input responses.

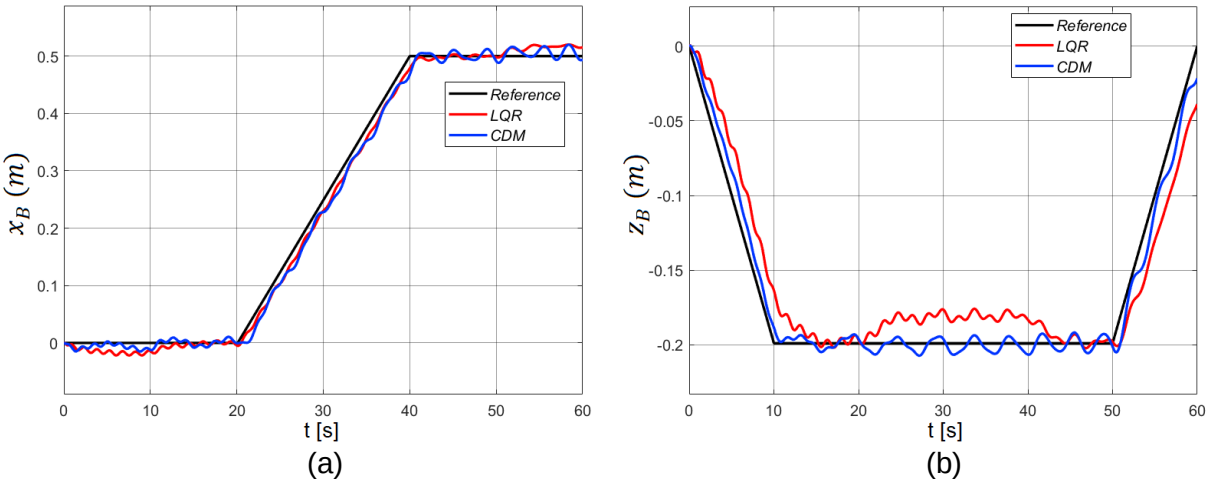

Figure 15: System responses with LQR and CMD methods (a) system response in the horizontal plane (b) system response in the vertical plane

Figure 15 shows the system's responses when the controller gains are calculated with the LQR method and the CDM. Steady-state errors arise at the LQR controller response between 0-10, 20-40, and 50-60 seconds. These are the instants when there is a reference input change. However, no significant steady-state error is observed with the CDM controller. The controller with the CDM has a faster response to the input changes. On the other hand, the effects of the disturbances on the system are observed more clearly with the CDM. As shown in Figure 15b, the amplitudes of the impacts of the disturbances are higher with CDM than with LQR.

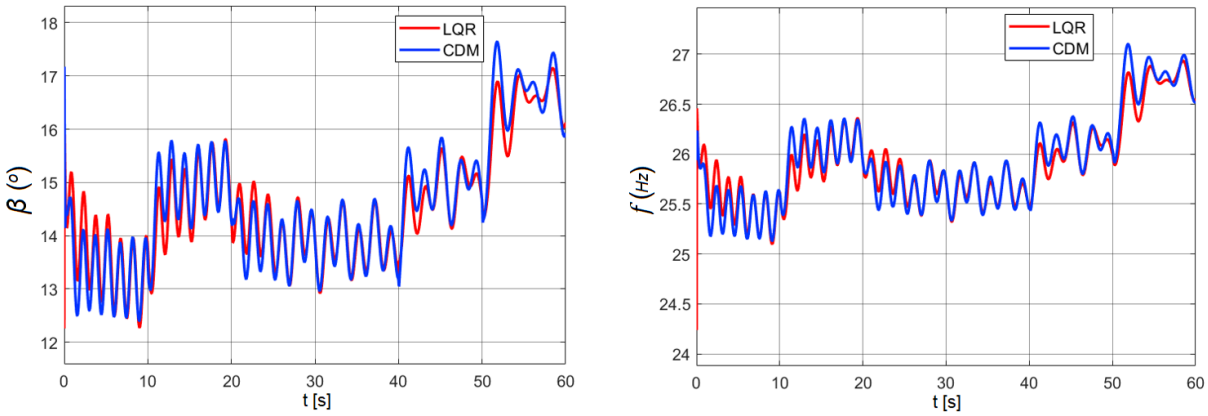

Figure 16: Response of the controllers to maintain the stability of the system and to track the reference inputs (a) Changes in the stroke plane angle (β) (b) Changes in the flapping frequency (f)

Figure 16 shows the controller responses of the two methods. With the CDM, slightly more aggressive responses are observed compared to the LQR controller.

CONCLUSION

The LQR controller and a controller with CDM are utilized to stabilize a flapping-wing MAV system. The employability of this type of controllers is proven for hovering and low speed flights in the existence of perturbative inputs. The controller with CDM tracked the position commands with better precision than the LQR controller but with a slightly more aggressive input effort. By adding integral trackers to the system, the system can track position commands in low-speed flights. The nonlinear wing model is included in the system, and this way, designing controllers and realizing simulations for different cases and objectives are possible. Since a flapping-wing MAV system's longitudinal and lateral dynamics are decoupled, by applying a similar control strategy also to the lateral dynamics, controlling a flapping-wing MAV in 3-D flight is possible.

ACKNOWLEDGEMENTS

This work is supported by TUBITAK 116M273 project.

References

Abbasi, S. H., and Mahmood, A. (2019) *Modeling, simulation and control of a bio-inspired electromechanical feather for gust mitigation in flapping wing UAV*. *International Conference on Communication,* Mar 2019

Akay, B., Kurtulus, D. F., and Alemdaroglu, N. (2007) *Unsteady aerodynamics of different wing profiles at low reynolds number*. NATO AVT-146 symposium on platform innovations and system integration for unmanned air, land and sea vehicles p: 14-17, May 2007

Al-Mahasneh, A. J., Anavatti, S. G., and Garratt, M. A. (2017) *Altitude identification and intelligent control of a flapping wing micro aerial vehicle using modified generalized regression neural networks.* IEEE Symposium Series on Computational Intelligence (SSCI) p: 1-6.

Banazadeh, A., and Taymourtash, N. (2016) *Adaptive attitude and position control of an insect-like flapping wing air vehicle.* Nonlinear Dynamics, 85(1), 47-66. Feb 2016

Bhatia, M., Patil, M., Woolsey, C., Stanfordx, B., and Beran, P. (2012) *Lqr controller for stabilization of flapping wing mavs in gust environments*. *AIAA Atmospheric Flight Mechanics Conference*, p: 4867, Aug 2012

Bektas, M., Guler, M. A., and Kurtulus, D. F. (2019) *Numerical investigation of a Hawkmoth wing undergoing pure plunge motion in hover.* Ankara International Aerospace Conference, Sep 2019

Bektas, M. (2020). *Biyo-esinlenmiş çırpan kanat modellerinin aeroelastik analizleri* (Master's thesis, TOBB ETÜ Fen Bilimleri Enstitüsü). Dec 2020

Bektas, M., Guler, M. A., and Kurtulus, D. F. (2020). *One-way FSI analysis of bio-inspired flapping wings*. International Journal of Sustainable Aviation, 6(3), 172-194, Dec 2020

Bhatia, M., Patil, M., Woolsey, C., Stanfordx, B., and Beran, P. (2012). *Lqr controller for stabilization of flapping wing mavs in gust environments.* AIAA Atmospheric Flight Mechanics Conference, p: 4867, Aug 2012

Biswal, S. (2015). *Modeling and control of flapping wing micro aerial vehicles*. Master's thesis, Arizona State University, May 2015

Biswal, S., Mignolet, M., and Rodriguez, A. A. (2019). *Modeling and control of flapping wing micro aerial vehicles.* Bioinspiration & biomimetics, 14(2), 026004.

Calis, O., Arikan, K. B., and Kurtulus, D. F. (2019) *CONTROL OF A FLAPPING WING MICRO AIR VEHICLE FOR NAVIGATION*, Ankara International Aerospace Conference, Sep 2019

Deng, X., Schenato, L., and Sastry, S. S. (2006). *Flapping flight for biomimetic robotic insects: Part II-flight control design.* IEEE Transactions on Robotics, 22(4), 789-803, Aug 2006

Giernacki, W., and Sadalla, T. (2017). *Comparison of Tracking Performance and Robustness of Simplified Models of Multirotor UAV's Propulsion Unit with CDM and PID Controllers (with anti-windup compensation).* J Control Eng App Inform, 19(3), 31-40.

Fei, F., Tu, Z., Yang, Y., Zhang, J., and Deng, X. (2019). *Flappy hummingbird: An open source dynamic simulation of flapping wing robots and animals*. International Conference on Robotics and Automation (ICRA) p: 9223-9229, May 2019

Han, J. S., and Han, J. H. (2019). *A contralateral wing stabilizes a hovering hawkmoth under a lateral gust.* Scientific reports, 9(1), 1-13.

Han, J. S., Kim, J. K., Chang, J. W., and Han, J. H. (2015*). An improved quasi-steady aerodynamic model for insect wings that considers movement of the center of pressure.* Bioinspiration & biomimetics, 10(4), 046014. July 2015

Hashemi, S. M., Botez, R. M., and Grigorie, L. T. (2020). *Adaptive fuzzy control of chaotic flapping relied upon lyapunov-based tuning laws.* AIAA AVIATION FORUM, p: 3193, June 2020

Hines, L. L., Arabagi, V., and Sitti, M. (2011). *Free flight simulations and pitch and roll control experiments of a sub-gram flapping-flight micro aerial vehicle*. IEEE International Conference on Robotics and Automation, p: 1-7, May 2011

Hirokawa, R., and Sato, K. (2004*). Lateral autopilot design for a UAV using coefficient diagram method.* International Congress of the Aeronautical Sciences, Aug 2004

Kara, S. E. (2014). *Control of Two Wheel Self Stabilizing Mobile Robot with a Simple Arm.* Master's thesis, Mechatronics Engineering, Atilim University, Oct 2014

Kim, J. K., and Han, J. H. (2013). *Control effectiveness analysis of the hawkmoth Manduca sexta: a multibody dynamics approach.* International Journal of Aeronautical and Space Sciences, 14(2), 152-161, May 2013

Kim, J. K., and Han, J. H. (2014). *A multibody approach for 6-DOF flight dynamics and stability analysis of the hawkmoth Manduca sexta.* Bioinspiration & biomimetics, 9(1), 016011, Jan 2014

Kim, J. K., Han, J. S., Lee, J. S., and Han, J. H. (2015). *Hovering and forward flight of the hawkmoth Manduca sexta: trim search and 6-DOF dynamic stability characterization.* Bioinspiration & biomimetics, 10(5), 056012, Sep 2015.

Kurtulus, D. F. (2009). *Ability to forecast unsteady aerodynamic forces of flapping airfoils by artificial neural network.* Neural Computing and Applications, 18(4), 359-368.

Kurtulus DF (2011) *Introduction to micro air vehicles: concepts, design and applications,* VKI LS 2011-04, Recent developments in unmanned aircraft systems, (UAS, including UAV and MAV), Ed. Carbonaro M., Decuypere R., ISBN-13 978-2-87516-017-1, p: 219-255, Apr 2011

Kurtulus, D. F. (2015). *On the unsteady behavior of the flow around NACA 0012 airfoil with steady external conditions at Re= 1000.* International Journal of Micro Air Vehicles, 7(3), 301-326, Sept 2015

Kurtulus, D. F. (2016). *On the wake pattern of symmetric airfoils for different incidence angles at Re= 1000.* International Journal of Micro Air Vehicles, 8(2), 109-139.

Kurtulus, D. F. (2018). *Aerodynamic loads of small-amplitude pitching NACA 0012 airfoil at Reynolds number of 1000.* AIAA Journal, 56(8), 3328-3331.

Kurtulus, D. F. (2019). *Unsteady aerodynamics of a pitching NACA 0012 airfoil at low Reynolds number.* International Journal of Micro Air Vehicles, 11, 1756829319890609, Nov 2019

Kurtulus DF, David L, Farcy A and Alemdaroglu N (2006a) *Aerodynamic Characteristics of Flapping Motion in Hover.* 13th Int Symp on Applications of Laser Techniques to Fluid Mechanics, 1130, Lisbon, Portugal, 26-29 June 2006.

Kurtulus DF, David L, Farcy A and Alemdaroglu N (2006b) *A Parametrical Study with Laser Sheet Visualization for an Unsteady Flapping Motion.* AIAA-2006-3917, AIAA Fluid Dynamics Conference and Exhibit, San Francisco, California USA, 5 - 8 June 2006.

Kurtulus DF, David L, Farcy A and Alemdaroglu N (2006c) *Laser Sheet Visualization for Flapping Motion in Hover.* AIAA-2006-0254, 44rd AIAA Aerospace Sciences Meeting and Exhibit, Reno, Nevada, USA, 9 - 12 Jan 2006.

Kurtulus, D. F., David, L., Farcy, A., and Alemdaroglu, N. (2008). *Aerodynamic characteristics of flapping motion in hover.* Experiments in Fluids, 44(1), 23-36.

Kurtulus, D. F., Farcy, A., and Alemdaroglu, N. (2004). *Numerical Calculation and Analytical Modelization of Flapping Motion in Hover.* In First European Micro Air Vehicle Conference and Flight Competition, Braunschweig Germany, p: 13-14, July 2004.

Kurtulus, D. F., Farcy, A., and Alemdaroglu, N. (2005). *Unsteady aerodynamics of flapping airfoil in hovering flight at low Reynolds numbers,* AIAA Aerospace Sciences Meeting and Exhibit, p: 1356, Jan 2005

Lee, J. S., Kim, J. K., and Han, J. H. (2015). *Stroke plane control for longitudinal stabilization of hovering flapping wing air vehicles.* Journal of Guidance, Control, and Dynamics, 38(4), 800-806, Apr 2015

Madangopal, R., Khan, Z. A., and Agrawal, S. K. (2006). *Energetics-based design of small flapping-wing micro air vehicles.* IEEE/ASME Transactions on Mechatronics, 11(4), 433-438, Aug 2006.

Manabe, S. (1998). *Coefficient diagram method.* IFAC Proceedings Volumes, 31(21), 211-222.

Nakatani, Y., Suzuki, K., and Inamuro, T. (2016). *Flight control simulations of a butterfly-like flapping wing–body model by the immersed boundary–lattice Boltzmann method.* Computers & Fluids, 133, 103-115.

P. Hyun, Nak-seung., McGill, R., Wood, R. J., and Kuindersma, S. (2021). *A new control framework for flapping-wing vehicles based on 3D pendulum dynamics.* Automatica, 123, 109293, Sept 2021

Sane, S. P., and Dickinson, M. H. (2002). *The aerodynamic effects of wing rotation and a revised quasi-steady model of flapping flight.* Journal of experimental biology, 205(8), 1087-1096, Jan 2002.

Stevens, B. L., Lewis, F. L., and Johnson, E. N. (2015). *Aircraft control and simulation: dynamics, controls design, and autonomous systems,* John Wiley & Sons, Nov 2015

Sun, M., and Xiong, Y. (2005). *Dynamic flight stability of a hovering bumblebee.* Journal of experimental biology, 208(3), 447-459, Nov 2004.

Taha, H. E., Hajj, M. R., and Nayfeh, A. H. (2012). *Flight dynamics and control of flapping-wing MAVs: a review.* Nonlinear Dynamics, 70(2), 907-939, July 2012.

Taylor, G. K., and Thomas, A. L. (2003). *Dynamic flight stability in the desert locust Schistocerca gregaria.* Journal of Experimental Biology, 206(16), 2803-2829, May 2003.

Ward, T. A., Fearday, C. J., Salami, E., and Binti Soin, N. (2017). *A bibliometric review of progress in micro air vehicle research.* International Journal of Micro Air Vehicles, 9(2), 1

Weis-Fogh, T. (1972). *Energetics of hovering flight in hummingbirds and in Drosophila.* Journal of Experimental Biology, 56(1), 79-104.

Willmott, A. P., and Ellington, C. P. (1997). *The mechanics of flight in the hawkmoth Manduca sexta. I. Kinematics of hovering and forward flight.* The Journal of experimental biology, 200(21), 2705-2722, Aug 1997.

Wissa, B. E., Elshafei, K. O., and El-Badawy, A. A. (2020). *Lyapunov-based control and trajectory tracking of a 6-DOF flapping wing micro aerial vehicle.* Nonlinear Dynamics, 99(4), 2919-2938.

Wright, J. R., and Cooper, J. E. (2008). *Introduction to aircraft aeroelasticity and loads* (Vol. 20). John Wiley & Sons.

Zhang, J., Cheng, B., and Deng, X. (2016). *Instantaneous wing kinematics tracking and force control of a high-frequency flapping wing insect MAV.* Journal of Micro-Bio Robotics, 11(1), 67-84.